Sensors and Actuators B 190 (2014) 40–47

Contents lists available at ScienceDirect

Sensors and Actuators B: Chemical

journal homepage: www.elsevier.com/locate/snb

Soft-chemical synthesis, characterization and humidity sensing behavior of WO_3/TiO_2 nanopowders

S.M. Zanetti[a,c,*], K.O. Rocha[a], J.A.J. Rodrigues[b], E. Longo[c]

[a] SENCER – Sensores Cerâmicos Ltda, Rua Santos Dumont, 800, 13566-445 São Carlos, SP, Brazil
[b] Laboratório Associado de Combustão e Propulsão, Instituto Nacional de Pesquisas Espaciais (INPE), Rodovia Presidente Dutra, Km 40, 12630-000 Cachoeira Paulista, SP, Brazil
[c] INCTMN – Instituto de Química, UNESP, Rua Francisco Degni, s/n, 14800-900 Araraquara, SP, Brazil

ARTICLE INFO

Article history:
Received 29 March 2013
Received in revised form 14 August 2013
Accepted 14 August 2013
Available online 29 August 2013

Keywords:
Polymeric precursor method
Chemical synthesis
WO_3/TiO_2
Humidity sensor
In situ XANES
EXAFS

ABSTRACT

Tungsten oxide/titania (WO_3/TiO_2) nanopowders were synthesized by the polymeric precursor method which varied the WO_3 content between 0 and 10 mol%. The powders were thermally treated in a conventional furnace and their structural, microstructural and electric properties were evaluated by X-ray diffraction (XRD), Raman spectrometry, N_2 physisorption, NH_3 chemisorption, temperature-programmed reduction (TPR), X-ray absorption near-edge spectroscopy (XANES) *in situ* XANES and extended X-ray absorption fine structure spectroscopy (EXAFS) and transmission electron microscopy (TEM). XRD and Raman spectrometry confirmed the homogeneous distribution of an amorphous WO_3 phase in the TiO_2 matrix which stabilized the anatase phase through the generation of $[TiO_5{\cdot}V_0^{\bullet}]$ or $[TiO_5{\cdot}V_0^{\bullet\bullet}]$ complex sites. Conventional TPR-H_2 (temperature programmed reduction) along with XANES TPR-H_2 and XANES TPR-EtOH showed that WO_3/TiO_2 sample reduction occurs through the formation of these complex clusters. Moreover, the addition of WO_3 promoted an increase in the surface acidity of doped samples as revealed by NH_3 chemisorption. The WO_3/TiO_2 bulk-ceramic samples were further used to estimate their potential application in a humidity sensor in the range of 15–85% relative humidity. Probable reasons that lead to the different humidity sensor responses of samples were given based on the structural and surface characterizations. Correlation between the sensing performance of the sensor and its structural features are also discussed. Although all samples responded as a humidity sensor, the W2T sample (2 mol% added WO_3) excelled for sensitivity due to the increase in acid sites, optimum mean pore size and pore size distribution.

1. Introduction

The coupling of titania with several semiconducting compounds has been extensively explored for photocatalytic property improvements. These coupled semiconductors include TiO_2–SnO_2 [1], TiO_2–ZnO [2] and WO_3–TiO_2 [3] among others. WO_3–TiO_2 compounds have attracted significant attention due to the addition of WO_3 to anatase which enhances both the photocatalytic activity and the sensory response [4,5].

Although the WO_3–TiO_2 system has been intensely studied as catalysts, there is a lack of data on its properties as sensors. Depero et al. [6] and Gerlich et al. [7] on this turn prepared TiO_2:WO_3 sensors with high WO_3 content (90% WO_3) for CO, CH_x, NO and NO_2. Chaudhari et al. [8] prepared TiO_2:WO_3-based gas sensors. They modified the TiO_2:15 wt%WO_3 composition with low concentration of Pt (0.5 wt%) in order to reach a highly sensitive, selective and reliable H_2 sensor.

Water detection remains an elusive target for sensory-specific measurements due to escalating demands for monitoring and controlling humidity in industrial and agricultural applications which constantly challenges sensing materials research. Ceramic sensors are based on the adsorption of water molecules into apertures and grain boundaries of porous semiconductors where internal surface conduction increases with humidity. Other advantages of ceramic sensors are their high resistance to chemical attack, thermal stability and mechanical strength. However, insufficient sensitivity over a wide humidity range in some types of sensing elements remains problematic. Among ceramic sensors, TiO_2 sensing materials are commonly researched due to easy fabrication.

Traversa et al. [9] have first studied the humidity sensitive electrical properties of sol–gel processed TiO_2 films. However, the performance of these films was not satisfactory for practical application due to the high intrinsic resistance at low humidity values

* Corresponding author at: INCTMN – Instituto de Química, UNESP, Rua Francisco Degni, s/n, 14800-900 Araraquara, SP, Brazil. Tel.: +55 16 3301 9771.
E-mail addresses: zanettism@gmail.com, zanetti@iq.unesp.br (S.M. Zanetti).

0925-4005/$ – see front matter © 2013 Elsevier B.V. All rights reserved.
http://dx.doi.org/10.1016/j.snb.2013.08.053

and limited sensitivity. Hence, several semiconducting oxides have been added to TiO_2 in order to diminish the resistance and increase the sensitivity of sensors. Faia et al. [10] prepared WO_3:TiO_2 films with different WO_3 content derived from powders of both oxides, TiO_2 and WO_3, as humidity sensors. They have proposed an explanation of the chemical and physical phenomena through the complex impedance data of a series of TiO_2–WO_3 thick films.

Various measuring techniques have been explored for humidity detection such as impedance [11,12], capacity [13], field effect transistors (FET) [14], quartz-crystal microbalance (QCM) [15,16] and microwave sensors [17]. Impedance-type humidity sensors (mainly for ceramics) have become more prevalent due to quality and cost considerations. Several techniques have been used for ceramic powder preparation, including conventional solid-state reactions, high-energy milling [18,19], self-combustion [20,21], co-precipitation [22,23], and chemical-solution processes.

Among the chemical solution processes, the polymeric precursor method has been successfully applied to produce ceramic sensors [24–26]. Moreover, microstructural properties of powders (*i.e.*, pore size, pore volume and surface area) can be tailored by controlling synthesis variables.

Nanoscale structures are able to enhance sensor response as in nanostructured powders. Improvements in sensory effectiveness have been demonstrated through nanoscale surface manipulation. In a previous study [27], WO_3–TiO_2 nanopowders were prepared by high-energy milling, and their ceramic properties were categorized as humidity sensors. As a physical method, high-energy milling successfully provided a nanosized powder; however, the obtained powder was not chemically homogeneous.

Herein, WO_3/TiO_2 nanopowders were chemically synthesized through the polymeric precursor method. The chemical synthesis promotes an intimate contact between the two oxides reaching an homogeneity in atomic level.

The aim of this research is the synthesis of chemically homogeneous WO_3/TiO_2 nanopowders by varying the WO_3 content, and investigating the influence of additive WO_3 on structural, microstructural and surface properties of TiO_2.

The WO_3/TiO_2 samples were further used to estimate their potential application in a humidity sensor. Probable reasons that lead to the different humidity sensor responses of samples were given based on the structural and surface characterizations. Correlation between the sensing performance of the sensor and its structural features are also discussed.

2. Experimental

2.1. Chemical synthesis

Titanium isopropoxide $Ti(OCH(CH_3)_2)_4$ (Aldrich, 97%), and tungstic acid, H_2WO_4 (Aldrich, 99%) were used as reagents for the synthesis of WO_3/TiO_2 compounds. Initially, titanium isopropoxide was dissolved in an aqueous citric acid (CA) solution at 60 °C under constant stirring to form titanium citrate at a CA/Ti molar ratio of 4. The Ti content was gravimetrically determined as TiO_2. Subsequently, W was stoichiometrically added to the titanium citrate solution by dissolving sufficient amounts of tungstic acid in an aqueous solution of NH_4OH to provide a ceramic oxide with 2, 5, and 10 mol% content of WO_3. Ethylene glycol (EG) was added after solution homogenization to promote mixed-citrate polymerization at a CA/EG mass ratio of 3/2.

The resin was kept on a hot plate until a viscous gel was formed which was subsequently thermally treated at 300 °C for 4 h in a furnace (WT precursor). The WT precursor was deagglomerated in an agate mortar and underwent thermal treatment at 400 °C for 4 h. The powder thus obtained was treated at 600 °C for 2 h in an electric furnace which completed the crystallization process. All thermal treatments were conducted at a heating rate of 10 °C min^{-1}. The samples were labeled according to their WO_3 content (see Table 1).

Table 1
Synthesized samples.

Sample	WO_3 (mol%)	TiO_2 (mol%)	Theoretical density (g cm^{-3})
W0T	0	100	3.89
W2T	2	98	3.96
W5T	5	95	4.06
W10T	10	90	4.24
W100T	100	0	7.39

2.2. Characterization

X-ray diffraction (XRD) measurements using a Rigaku D/Max 2500 (40 kV, 100 mA) were conducted to follow the crystalline phases with Cu Kα radiation at room temperature. Average crystallite sizes (D) for the samples were estimated by the Scherrer equation:

$$D = \frac{K\lambda}{\beta \cdot \cos\theta\,(\mathrm{nm})} \quad (1)$$

where β is the line-broadening at half-height width of the anatase diffraction peak ($2\theta \sim 25.5°$), K is a coefficient (0.89), λ is the Cu Kα radiation wavelength, and θ is the diffraction angle. Raman spectra in the range of 100–1000 nm were obtained with a BRUKER spectrometer (FRA-106/S) using the 1064 nm excitation line of an Nd–YAG Laser. Data were recorded at room temperature with the power at 60 mW, 100 scans and 4 cm^{-1} resolution. XANES spectra at the W L3-edge (10.207 KeV) were measured at the D06A-DXAS beamline of the LNLS. The D06A-DXAS is a dispersive beamline equipped with a focusing curved Si(1 1 1) monochromator operating in Bragg mode that selects the X-ray energy-bandwidth which incorporates a 1152 × 1242 (500 × 900) pixel CCD solid-state detector and converts X-rays into visible light for spectral analysis. Samples were formed into self-supporting pellets and placed into a tubular quartz furnace sealed with kapton for transmission measurements. *In situ* XANES TPR-H_2 spectra were acquired during the TPR treatment of W2T samples treated at 600 °C for 2 h under a 30 mL min^{-1} H_2:He flow (5:95) at up to 600 °C while *in situ* XANES TPR-EtOH spectra were acquired during the TPR treatment of a W10T sample treated at 600 °C for 2 h under 300 mL min^{-1} N_2-saturated ethanol flow at 20 °C up to a 400 °C maximum. Emitted gases were analyzed by an on-line mass spectrometer. Surface characteristics were studied by TPR-H_2 using 5% H_2/N_2 and NH_3 pulse chemisorptions; measurements were performed using a Micrometrics Pulse ChemiSorb 2707. Metrics for pore distribution and pore size were examined by N_2 adsorption/desorption BET isotherms (Micromeritics, ASAP 2000). The mean particle size was determined from surface area values measured by N_2 adsorption/desorption isotherms *via* the equation:

$$\mathrm{MPS_{BET}} = \frac{6000}{\rho \cdot S_{\mathrm{BET}}} \quad (2)$$

where $\mathrm{MPS_{BET}}$ is the mean particle size (nm), ρ is the theoretical density, and S_{BET} is the surface area. The powder morphology from various temperature treatments was examined by TEM (JEOL 6400).

2.3. Characterization of humidity sensor properties

Sensor elements were prepared as pellets (10 mm diameter and 2 mm thick) obtained by uniaxial compression (0.5 ton load) of powder treated at 400 °C for 2 h. Pellets were treated at 600 °C for 2 h, and a silver coating was deposited on both pellet faces to form the electrodes. Sensor elements were subjected to humidity

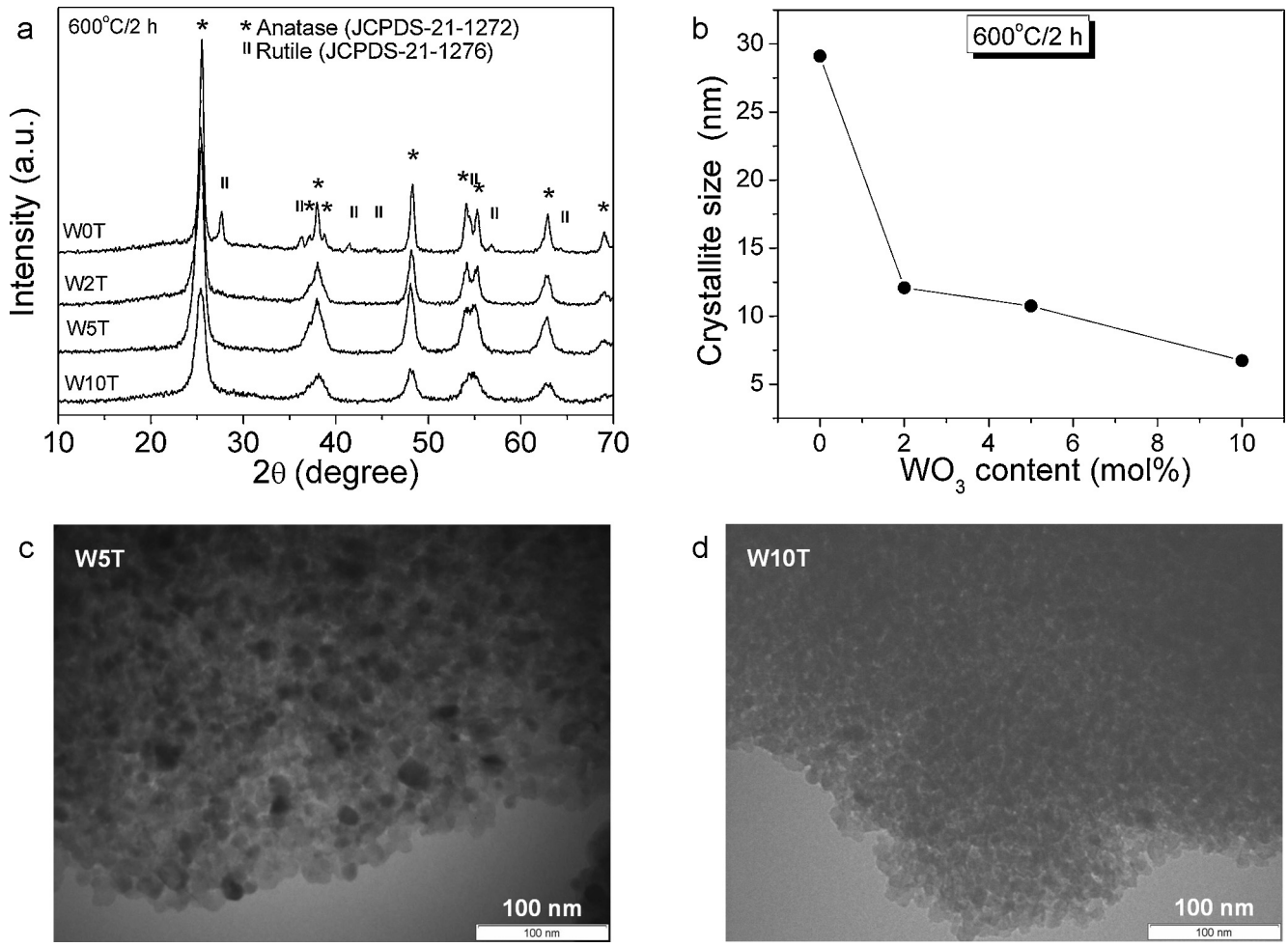

Fig. 1. (a) XRD patterns of WT powders; (b) crystallite size as a function of WO_3 content; (c) and (d) TEM images of W5T and W10T powders treated at 600 °C for 2 h, respectively.

levels of 15–85% RH at 10% increments in a calibration humidity chamber (Biothec–BT 2001) maintained at 25 °C, and their electrical response was measured using a LCR (Agilent E4980A – 20 – 2 MHz) device at 1 kHz.

3. Results and discussion

Fig. 1a shows XRD profiles of WT samples treated at 600 °C for 2 h. The W0T sample XRD pattern (without the addition of WO_3) showed peaks related to TiO_2 as anatase and rutile phases. The addition of WO_3 suppressed the formation of the rutile phase even at a low WO_3 content level. According to Yang et al. [28], the anatase phase is stable due to oxygen vacancies. If W^{6+} ions are added to a TiO_2 matrix, the valence state in the Ti^{4+} neighborhood will be reduced, and extra oxygen vacancies will be created which increases the number of these defects and stabilizes the TiO_2 in the anatase phase. Note that doped sample XRD patterns did not show peaks related to the tungsten oxide phase even with a 10 mol% WO_3 content level which indicates that WO_3 is present as an amorphous phase. The broadening of anatase peaks with the incorporation of tungsten oxide indicates a decrease in the crystallite size. The TiO_2 anatase crystallite size as calculated by the Scherrer equation decreased from approximately 29 nm (for the W0T sample) to 7 nm (for the W10T sample). TEM images of W5T (see Fig. 1c) and W10T (see Fig. 1d) samples reveal the same behavior for the mean particle size as well.

Raman spectra for WT samples (see Fig. 2) were recorded to observe the short-range crystalline order. For W0T, the TiO_2 anatase phase is associated with bands at 145 cm^{-1} (E_g), 195 cm^{-1} (E_g), 396 cm^{-1} (B_{1g}), 516 cm^{-1} (A_{1g}) and 639 cm^{-1} (E_g) [29]), and the rutile phase is associated with the band at 448 cm^{-1} and a shoulder at 610 cm^{-1} [27]). The addition of WO_3 caused bands related

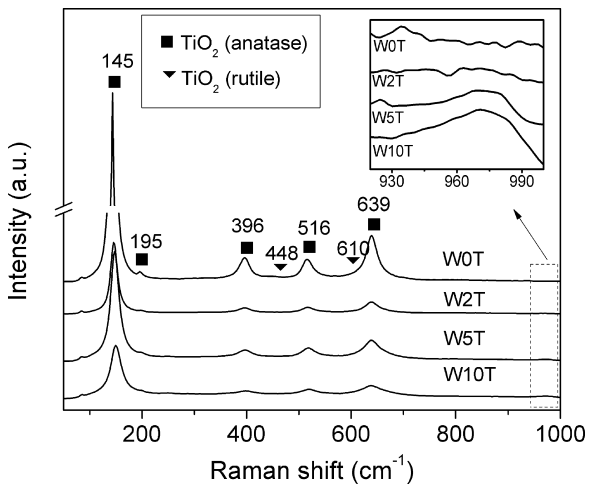

Fig. 2. Raman spectra of WT samples treated at 600 °C for 2 h.

Table 2
Wavenumber (cm^{-1}) and the FWHM (in parenthesis) of samples treated at 600 °C for 2 h.

	E_g (cm^{-1})	E_g (cm^{-1})	B_{1g} (cm^{-1})	A_{1g} (cm^{-1})	E_g (cm^{-1})
W0T	143 (11.3)	195 (12.3)	395 (23.6)	515 (24.6)	638 (23.6)
W2T	145 (13.1)	196 (16.7)	395 (25.2)	516 (25.1)	638 (27.5)
W5T	148 (21.1)	196 (18.8)	398 (30.7)	519 (30.1)	637 (37.7)
W10T	146 (18.8)	194 (23.8)	397 (27.8)	516 (22.3)	638 (31.3)

to the rutile phase to disappear and thus confirms XRD results. No bands associated with the WO_3 phase, at 715 cm^{-1} and 805 cm^{-1} were observed which indicates that small clusters of WO_3 could be a well dispersed amorphous phase in the TiO_2 matrix; in agreement with XRD results. The graphic inset in Fig. 2 shows a band around 970 cm^{-1} for samples with a WO_3 content higher than 5 mol% which is ascribed to W=O bonds formed on tungsten ions with low coordination, as in amorphous WO_3. Similar results were observed by Akurati et al. [3].

Table 2 lists the FWHM (full width at half maximum) and wavenumber for bands observed in the anatase phase in Raman spectra.

The shift to higher band wavenumbers at 143 cm^{-1} of the W0T sample compared with doped samples was noted. This shift to a higher wavenumber may be associated with a decrease in crystallite size. According to Ref. [30], when the particle size decreases to a nanometer scale, a volume contraction occurs within the nanoparticle due to size-induced radial pressure which produces an increase in force constants as a result of the decrease in interatomic distances. W10T was expected to shift to a higher wavenumber and continue increasing when the particle size decreased. However, the Raman result for this sample suggests a decrease in the short-range disorder in comparison with W5T which is possibly associated with changes in the Ti neighborhood due to a higher amorphous WO_3 content.

XAS (X-ray absorption spectroscopy) measurements were carried out to observe chemical alterations in the compounds. The Fourier transformed EXAFS oscillations for pure TiO_2 and doped samples treated at 600 °C for 2 h showed the first peak at $1 < R < 2$ corresponding to the first oxygen coordination shell around Ti (Ti–O1 at 1.937 Å and Ti–O2 at 1.966 Å), and the subsequent peak between $2 < R < 3$ corresponding mainly to a Ti–Ti second coordination shell (3.039 Å) (see Supplementary File). Table 3 lists the coordination number (CN), inter-atomic distance (r), Debye–Waller factor ($\Delta\sigma^2$) and R factor for the first coordination shell scattering of TiO_2 for the WT samples treated at 600 °C for 2 h.

EXAFS results indicate that the W0T sample (TiO_2) has a lower coordination number (5.07) in comparison with commercial TiO_2 (5.91) [27] which may be attributed to the nanostructured powder achieved by the polymeric precursor method. Additional WO_3 produced slightly decreased coordination numbers for W2T and W5T samples and increased values for the W10T in comparison with W0T. These results are in agreement with Raman results; therefore, the shift in the wavenumber is possibly correlated to the Ti–O coordination shell. The reason for this coordination number decrease as well as for the shift in the Raman wavenumber up to 5 mol% WO_3 content may be associated with the formation of two different kinds of clusters, $[TiO_6]^x$ and $[WO_6]^{\bullet\bullet}$.

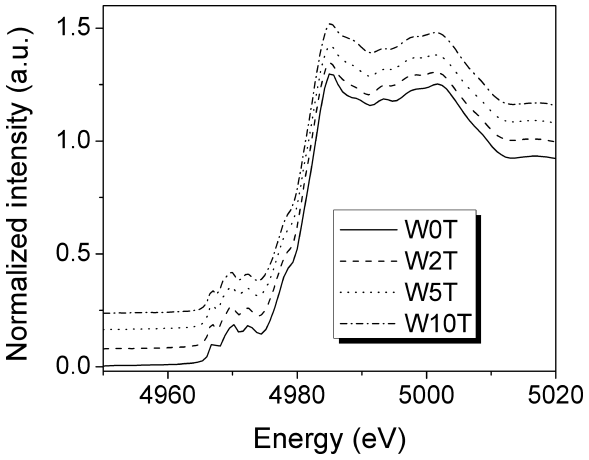

Fig. 3. XANES region spectra of WT samples treated at 600 °C for 2 h.

According to Longo et al. [31] TiO_2 powders may display two types of environments for the titanium, namely, a fivefold $[TiO_5]$ square-based pyramid and a sixfold coordination $[TiO_6]$ octahedron. In the $[TiO_5]$ complex cluster, Ti is surrounded by five oxygens in a square-based pyramidal configuration. In titanates, oxygen vacancies can occur in three different charge states: (a) the $[TiO_5{\cdot}V_0{}^x]$ complex states which have captured paired electrons and are neutral relative to the lattice; (b) the singly ionized $[TiO_5{\cdot}V_0{}^{\bullet}]$ complex state, which has one unpaired electron; and (c) the $[TiO_5{\cdot}V_0{}^{\bullet\bullet}]$ complex state, which did not trap any electrons and is doubly positively charged with respect to the lattice [32].

The increase in the W10T coordination number could correspond to an increase of $[WO_6]^{\bullet\bullet}$ cluster contents (not detected by XRD or Raman) which restricted the formation of $[TiO_6]^x$ and $[TiO_5{\cdot}V_0{}^x]$ complex clusters according to the following equations [31–33]:

$$[TiO_6]^x \rightarrow [TiO_6]^I + [TiO_5{\cdot}V_0{}^{\bullet}] \quad (3)$$

$$[TiO_6]^x + [TiO_5{\cdot}V_0{}^{\bullet}] \rightarrow [TiO_6]^I + [TiO_5{\cdot}V_0{}^{\bullet\bullet}] \quad (4)$$

$$[WO_6]^{\bullet\bullet} + 2[TiO_6]^I \rightarrow 2[TiO_6]^x + [WO_6]^x \quad (5)$$

where $[TiO_5{\cdot}V_0{}^{\bullet}]$, $[TiO_5{\cdot}V_0{}^{\bullet\bullet}]$ and $[TiO_6]^I$ are complex clusters.

In spite of the coordination number decrease with WO_3 doping, the interatomic distance did not change. Thus, no alteration in the electronic density was observed for TiO_2 nanoparticles. The WL (white line) intensity variation in the XANES region did not show any alteration of electronic density (see Fig. 3).

Table 3
Structural parameters obtained by EXAFS for WT samples treated at 600 °C for 2 h and reference (TiO_2).

Sample	Scattering	CN	r (Å)	$\Delta\sigma^2$ (Å^2)	R factor
TiO_2 [22]	Ti—O	5.91 ± 0.06	1.95 ± 0.01	0.005	0.03
W0T	Ti—O	5.07 ± 0.05	1.94 ± 0.05	0.005	0.03
W2T	Ti—O	4.98 ± 0.06	1.95 ± 0.04	0.005	0.03
W5T	Ti—O	5.04 ± 0.07	1.95 ± 0.04	0.005	0.03
W10T	Ti—O	5.32 ± 0.06	1.95 ± 0.03	0.005	0.03

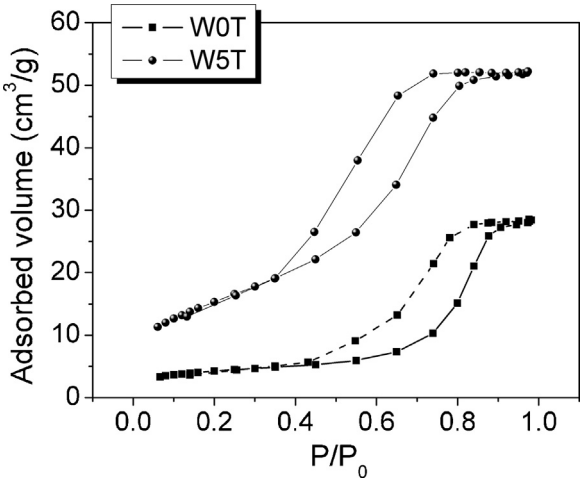

Fig. 4. N_2 adsorption isotherms of W0T and W5T samples treated at 600 °C.

Although the concentration of $[TiO_5{\cdot}V_0^{\bullet}]$ and $[TiO_5{\cdot}V_0^{\bullet\bullet}]$ complex clusters may have increased with WO_3 doping, no alteration in the electronic structure was observed by XAFS and XANES data which indicates that W was not incorporated into the TiO_2 structure but remained as an amorphous phase as observed by XRD and Raman results. Therefore, Raman data may be explained by the alteration in oxygen stoichiometry observed in the EXAFS region.

The influence of additional WO_3 on the microstructure of samples was observed through N_2 adsorption isotherms. Isotherms for W0T and W5T samples treated at 600 °C for 2 h are displayed in Fig. 4. Isotherm profiles for W2T and W10T samples are identical and thus, are not shown here.

Type IV isotherms shown in Fig. 4 are characteristics of organic–inorganic nanocomposites with accessible mesopores. H1 hysteresis loops are often typical for agglomerates (assemblages of rigidly joint particles) materials or compacts of approximately spherical particles arranged in a approximately uniform way. Recently, it has become clear that H1 hysteresis loops are also characteristic of materials with cylindrical-pore geometry and a high degree of pore size uniformity. Thus, the H1 hysteresis loop in the adsorption isotherm for a porous solid generally indicates a relatively high pore size uniformity and facile pore connectivity [34].

The pore size distribution illustrated in Fig. 5a supports the type of isotherm and hysteresis loop discussed above for mesopore parameters [35]. The WO_3 content increase produces a pore size distribution at a micropore range and decreased distribution breadth. The narrowest pore size distribution was observed in the W10T sample. Fig. 5b confirms that the surface area increases with the addition of WO_3 and resulted in an expected corresponding decrease in both the pore mean diameter and the mean particle size.

Surface characteristics were studied by TPR-H_2 and NH_3 pulse chemisorption. Fig. 6 shows TPR-H_2 WT sample profiles treated at 600 °C for 2 h. TPR-H_2 results were analyzed based on TPR peak deconvolution below 1000 °C.

The W0T sample (see Fig. 6a) reveals broad peaks at 248 °C, 482 °C, 586 °C, 648 °C, 845 °C, and 941 °C. With the addition of 2 mol% of WO_3 (W2T sample) (see Fig. 6b), the TPR profile depicted broad peaks at 447 °C, 580 °C, 651 °C, 689 °C and 760 °C. The W5T sample (see Fig. 6c) showed peaks at 399 °C, 499 °C, 595 °C and 674 °C. The W10T sample (see Fig. 6d) manifested peaks at 515 °C, 576 °C, 644 °C, 687 °C, 728 °C and 758 °C. Three primary peaks for W100T (which contains only WO_3) (see Fig. 6e) were observed at 770 °C, 826 °C and 915 °C.

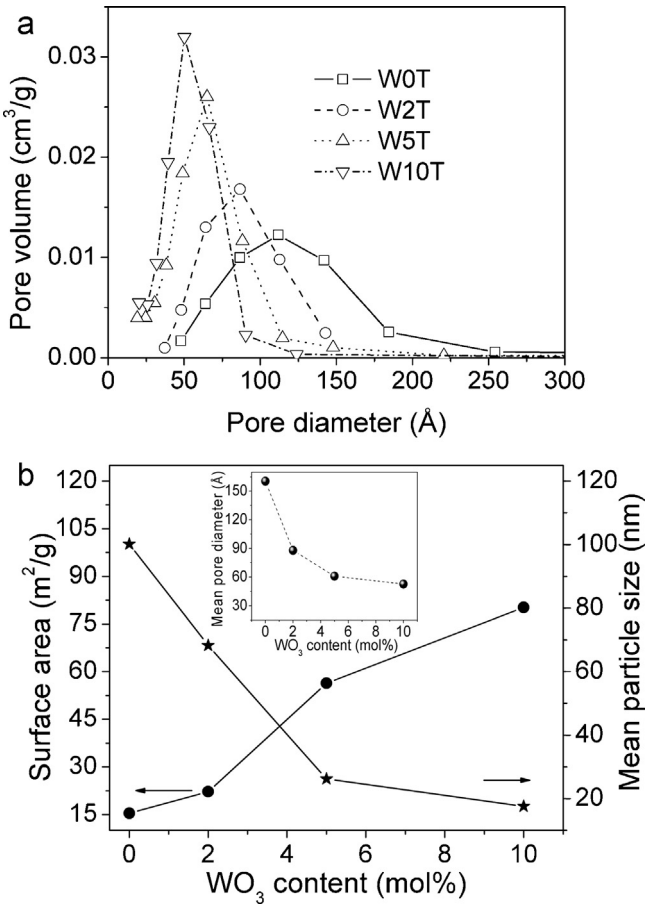

Fig. 5. (a) Pore size distribution; (b) surface area and mean pore diameter (Inset: Mean particle size) of WT samples treated at 600 °C as a function of WO_3 content.

These results illustrate that the addition of WO_3 promotes the shift of TPR peaks to lower temperatures along with the appearance of new peaks. Moreover, the peaks intensify which suggests an increase of the available sites for reduction attributable to a decrease in crystallite and particle sizes as observed in XRD and N_2 adsorption (BET), respectively. Additionally, the reduction profile time was extended at 1000 °C, probably due to the

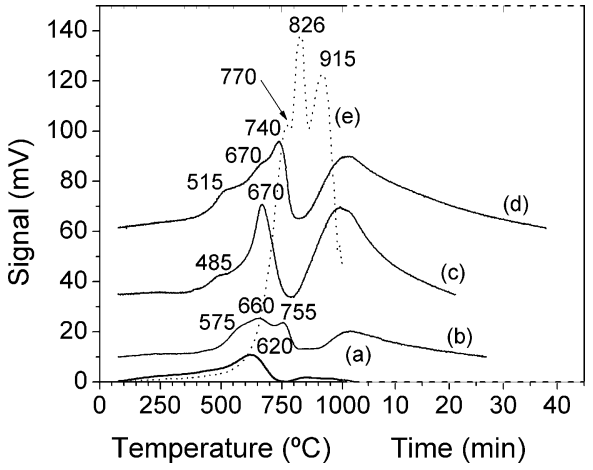

Fig. 6. TPR-H_2 of samples treated at 600 °C for 2 h: (a) W0T; (b) W2T; (c) W5T; (d) W10T and (e) W100T (WO_3 only). The dashed line at the horizontal axis corresponds to the soaking period at 1000 °C.

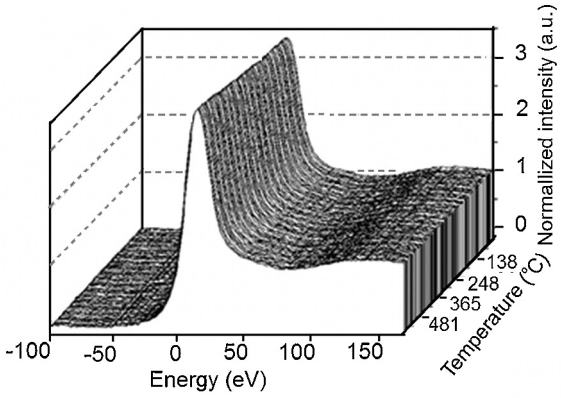

Fig. 7. *In situ* XANES TPR-H_2 of W2T sample.

decreasing in particle size. The reduction of TiO_2 is observed by some authors [36–38] possibly attributed to $[TiO_6]^x \rightarrow [TiO_5{\cdot}V_0{}^x]$, $[TiO_5{\cdot}V_0{}^{\bullet}]$ or $[TiO_5{\cdot}V_0{}^{\bullet\bullet}]$ transitions. However, since the pure WO_3 sample (W100T) also exhibited H_2 consumption peaks, an *in situ* XANES TPR was conducted to accurately analyze the profile for reduced samples.

Fig. 7 shows the *in situ* XANES TPR-H_2 for the W2T sample. No change due to the H_2 treatment was observed in WL intensity of the W L_3 edge until 600 °C. The WL intensity change is related to an electron transition from a filled-orbital $2p_{3/2}$ to a half-filled orbital $5d_{5/2}$ (a transition that obeys the selection rule) and reflects empty valence state levels. The higher the oxidation state, the more intense the WL reading as previously observed for Ni [39,40] and Pt [41] catalysts. Although no variation of the oxidation state of W was observed by XANES, the conventional TPR of the W2T sample showed a consumption of H_2 attributable to $[TiO_6]^x \rightarrow [TiO_5{\cdot}V_0{}^x]$, $[TiO_5{\cdot}V_0{}^{\bullet}]$ or $[TiO_5{\cdot}V_0{}^{\bullet\bullet}]$ which suggests that TiO_2 is really a reducible oxide as considered by other authors [36–38].

An effective reducing agent, ethanol, was employed to analyze the reduction profile to enhance the assumption of Ti reduction. Fig. 8a shows the *in situ* XANES TPR-EtOH for the W10T sample. Again, no WL intensity change of the W L_3 edge was observed in accordance with the *in situ* XANES TPR-H_2 profile. However, on-line mass spectra of the *in situ* XANES TPR-EtOH showed the formation of H_2 at approximately 350 °C (see Fig. 8b). The production of H_2 (with ethanol) is possible only if metallic sites are formed [42,43]. Hence, if no change was observed in the WO_3 electronic structure which reveals the formation of W^0, the metallic sites are a product of TiO_2 reduction. Obviously, due to its nature, ethanol reduces TiO_2 before H_2 reduction.

Thus, the H_2 consumption peak observed in the conventional TPR (see Fig. 6) may be attributed to the formation of complex cluster sites. The reduction process initially occurs in sites with a lower coordination number (or higher electronic density) as sites in steps or corners ($[TiO_5{\cdot}V_0{}^{\bullet}]$ or $[TiO_5{\cdot}V_0{}^{\bullet\bullet}]$ complex clusters) which activate H_2 more easily. After these sites have been reduced, a subsequent reduction is facilitated by a spill-over process which is observable for a W0T sample through a peak at 517 °C followed by a peak at 628 °C.

Table 4 displays the acidity determined by NH_3 chemisorption of samples treated at 600 °C. The TiO_2 acidity per mol gradually increased with the addition of WO_3 as also reported by Akurati [3]. The abrupt increase in acidity for W10T may be correlated with the formation of small WO_3 clusters which chemisorbs the NH_3 as, observed for W100T. These results confirm that WO_3 is an amorphous phase deposited on the TiO_2 matrix surface as previously discussed.

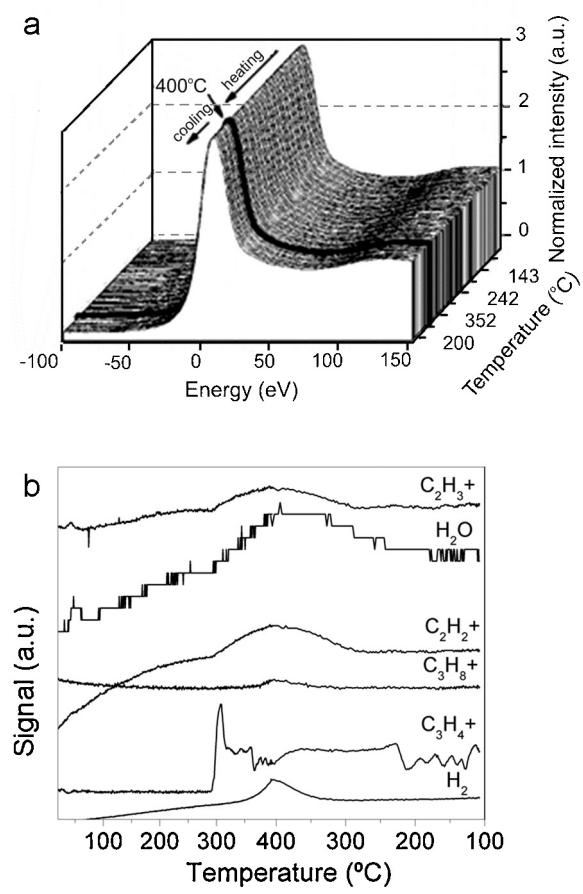

Fig. 8. (a) *In situ* XANES TPR-EtOH; (b) on-line mass spectra signal of the *in situ* XANES TPR-EtOH for the W10T sample.

Surface characteristics for WT samples obtained by the polymeric precursor method revealed the potentiality of these samples to act as sensors. To observe the performance of WT samples as humidity sensors, the electrical resistance of WT sensor elements was measured as a function of the relative humidity (RH) at 1 kHz in a climatic chamber maintained at 25 °C.

Fig. 9a shows the W0T sample with a linear response along the entire RH (relative humidity) range in spite of low sensitivity and hysteresis values. The addition of 2 mol% WO_3 did not change the low hysteresis observed for the W0T sample, but it did increase the sensitivity. The humidity sensitivity in the 15–85% RH range (defined as $S = \Delta R/\Delta RH$) was 277 $k\Omega\,\%^{-1}$ for W0T and 7070 $k\Omega\,\%^{-1}$ for W2T (see Fig. 9b). The sensitivity increase may be attributed to an acidity increase as previously discussed along with a decrease in the mean pore diameter.

A significant diminishing in electrical resistance is probably due to an increase in $[TiO_5{\cdot}V_0{}^x]$, $[TiO_5{\cdot}V_0{}^{\bullet}]$ or $[TiO_5{\cdot}V_0{}^{\bullet\bullet}]$ clusters sites (according to Eqs. (3)–(5)) for W5T and W10T samples. Although the addition of 5% and 10% WO_3 promoted an increase in acid sites, there was a concurrent decrease in the mean pore diameter and a reduced pore diameter distribution (see Fig. 5a) which resulted in

Table 4
Acidity of WT samples as determined by NH_3 pulse chemisorption.

Sample	Acidity (μmol NH_3/g_{sample})	Acidity (mol NH_3/mol TiO_2)
W0T	264.1	0.2
W2T	286.0	0.4
W5T	294.1	0.5
W10T	795.1	6.13
W100T	112.7	–

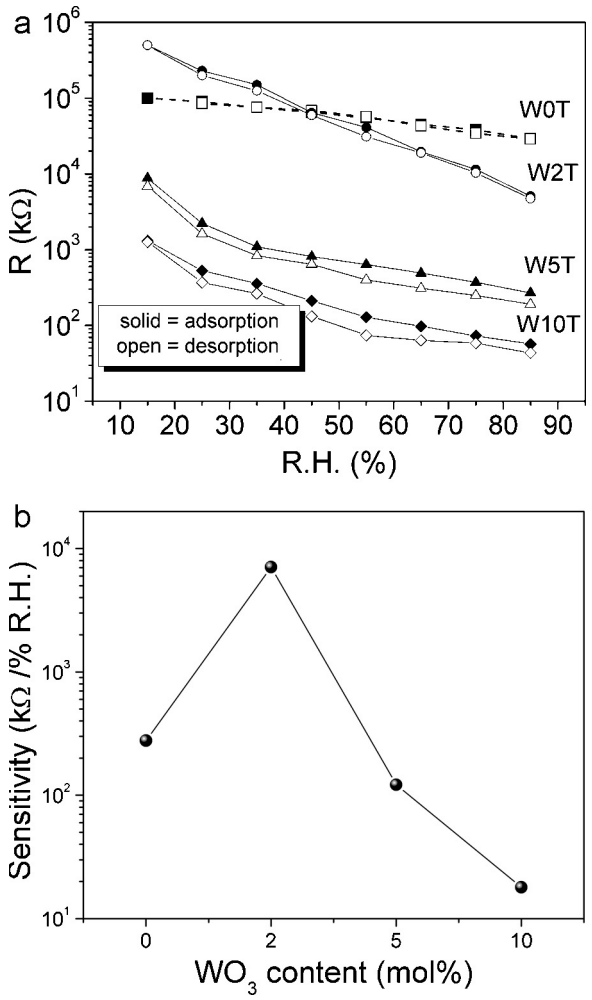

Fig. 9. Resistance as a function of RH (a) and sensitivity (b) for WT samples treated at 600 °C for 2 h.

a higher sensitivity observed in low RH ranges (15–35% RH). An RH increase (with pore filling) resulted in capillary condensation with a consequent decrease in sensitivity in higher RH levels.

Considering the combination of sites of positive character (acids sites), water molecules dissociated on the sensor surface and the formation of a chemically adsorbed first layer, one can infer that a greater number of acid sites increases the sensor element sensitivity as observed for W2T sample.

According to these results, WT samples can be considered as a core–shell-like structure (TiO_2@WO_3) where TiO_2 particles are involved by amorphous WO_3 which creates a heterojunction. The effect of surface properties on sensor performance should be considered in terms of $[TiO_6]_o$ and $[WO_6]_d$ clusters where o = order and d = disorder. Structural and density variations of defects in the interfacial region might be responsible for the TiO_2@WO_3 sensor behavior. Complex clusters often behave as an electron sink and improve charge separation within the semiconductor sensor system. These electrons can be discharged to the acceptor H_2O at the interface. Consequently, the effect of sensor surface properties should be considered in terms of the reactions described in Eqs. (6)–(7). The complex clusters formed interact with water and separate it into its hydroxyl radicals and hydrogen ions in terms of the following reactions:

$$[TiO_5{\cdot}V_0^{\bullet}] + H_2O_{(ads)} \rightarrow [TiO_5{\cdot}V_0^{x}]^{\bullet\bullet\bullet}OH*_{(ads)} + H^{\bullet}_{(ads)} \quad (6)$$

$$[TiO_5{\cdot}V_0^{\bullet\bullet}] + H_2O_{(ads)} \rightarrow [TiO_5{\cdot}V_0^{x}]^{\bullet\bullet\bullet}OH*_{(ads)} + H^{\bullet}_{(ads)} \quad (7)$$

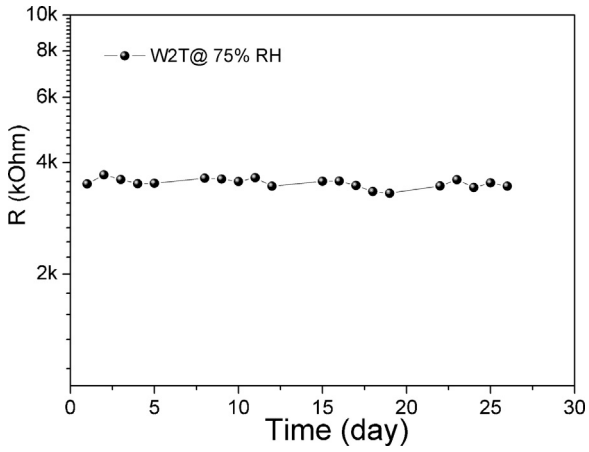

Fig. 10. Stability of the W2T-based humidity sensor at 75% RH over 4 weeks measured at 1 kHz and 1 V.

On the other hand, pore diameter distribution is an additional important factor in water adsorption which produces capillary condensation and decreases sensitivity; this phenomenon was observed for W5T and W10T samples. Also, the pore size (in the micropore range) and pore distribution attained in these samples are possibly responsible for the hysteresis observed in Fig. 9a. The introduction of tungsten in anatase is known to act as an electron acceptor [4] which explains a decrease in resistance of those samples.

The stability of the W2T sample was evaluated by measuring every day the resistance of the sensor kept in a chamber at 75% RH (reached using saturated solution of NaCl salt) for 4 weeks, as can be observed in Fig. 10. Acceptable change of about 3% in the resistance was observed over time until 15 days, indicating that the long-time stability is good enough for practical use. For longer time, a drift in resistance of about 15% is observed, probably due to the gradual formation of stable chemisorbed OH^- on the oxide surface for prolonged exposure to humid environments. The sensor properties can be recovered by a periodic heat cleaning at temperatures about 400 °C [9].

4. Conclusion

Results to date support the conclusion that the addition of WO_3 to TiO_2 by the polymeric precursor method produces a chemical homogeneous powder. The homogeneous distribution of WO_3 in a TiO_2 matrix stabilizes the anatase phase as confirmed by XRD and Raman spectroscopy. Moreover, then addition of WO_3 creates $[TiO_5{\cdot}V_0^{\bullet}]$ or $[TiO_5{\cdot}V_0^{\bullet\bullet}]$ sites up to 5 mol% WO_3 content. Results of conventional TPR-H_2 along with XANES TPR-H_2 and XANES TPR-EtOH infer a reduction of WO_3/TiO_2 samples which occurs through the formation of complex clusters, facilitated by an increased quantity of $[TiO_5{\cdot}V_0^{\bullet}]$ or $[TiO_5{\cdot}V_0^{\bullet\bullet}]$ sites. EXAFS results confirmed that the Raman band shift at 143 cm^{-1} is attributable to environmental oxygen in the neighborhood of Ti; all samples responded as humidity sensors. Considering sensitivity, the optimal sample was W2T (2 mol% WO_3 added) due to the increase in acid sites and optimum mean pore size and as well as the pore size distribution.

Acknowledgements

The authors gratefully acknowledge LNLS/Campinas – SP for the EXAFS (proposal D04B-XAFS1-9777) and XANES (proposal D06A-DXAS-11007) analysis on beam lines equipment and to CNPq for the financial support.

Appendix A. Supplementary data

Supplementary data associated with this article can be found, in the online version, at http://dx.doi.org/10.1016/j.snb.2013.08.053.

References

[1] C. Ribeiro, E. Longo, E.R. Leite, Tailoring of heterostructures in a SnO_2/TiO_2 system by the oriented attachment mechanism, Appl. Phys. Lett. 91 (2007) 103105.
[2] R. Liu, H. Ye, X. Xiong, H. Liu, Fabrication of TiO_2/ZnO composite nanofibers by electrospinning and their photocatalytic property, Mater. Chem. Phys. 121 (3) (2010) 432–439.
[3] K.K. Akurati, A. Vital, J.-P. Dellemann, K. Michalow, T. Graule, D. Ferri, A. Baiker, Flame-made WO_3/TiO_2 nanoparticles: Relation between surface acidity, structure and photocatalytic activity, Appl. Catal. B 79 (1) (2008) 53–62.
[4] S.A.K. Leghari, S. Sajjad, F. Chen, J. Zhang, WO_3/TiO_2 composite with morphology change via hydrothermal template-free route as an efficient visible light photocatalyst, Chem. Eng. J. 166 (3) (2011) 906–915.
[5] Y. Zhu, X. i Su, C. Yang, X. Gao, F. Xiao, J. Wang, Synthesis of TiO_2–WO_3 nanocomposites as highly sensitive benzene sensors and high efficiency adsorbents, J. Mater. Chem. 22 (2012) 13914–13917.
[6] L.E. Depero, M. Ferroni, V. Guidi, G. Marca, G. Martinelli, P. Nelli, L. Sangalettia, G. Sberveglieri, Preparation and micro-structural characterization of nanosized thin film of TiO_2–WO_3 as a novel material with high sensitivity towards NO_2, Sens. Actuators B 35–36 (1996) 381–383.
[7] M. Gerlich, S. Kornely, M. Fleischer, H. Meixner, R. Kassing, Selectivity enhancement of a WO_3/TiO_2 gas sensor by the use of a four-point electrode structure, Sens. Actuators B 93 (2003) 503–508.
[8] G.N. Chaudhari, A.M. Bende, A.B. Bodade, S.S. Patil, V.S. Sapkal, Structural and gas sensing properties of nanocrystalline TiO2:WO3-based hydrogen sensors, Sens. Actuators B 115 (2006) 297–302.
[9] E. Traversa, G. Gnappi, A. Montenero, G. Gusmano, Ceramic thin films by sol–gel processing as novel materials for integrated humidity sensors, Sens. Actuators B 31 (1996) 59–70.
[10] P.M. Faia, C.S. Furtado, A.J. Ferreira, Humidity sensing properties of a thick-film titania prepared by a slow spinning process, Sens. Actuators B 101 (2004) 183–190.
[11] J. Wang, M.-Y. Su, J.-Q. Qi, L.-Q. Chang, Sensitivity and complex impedance of nanometer zirconia thick film humidity sensors, Sens. Actuators B 139 (2009) 418–424.
[12] J.G. Lee, S.P. Lee, Impedance characteristics of carbon nitride films for humidity sensors, Sens. Actuators B 117 (2006) 437–441.
[13] P.-G. Su, C.-S. Wang, In situ synthesized composite thin films of MWCNTs/PMMA doped with KOH as a resistive humidity sensor, Sens. Actuators B 124 (2007) 303–308.
[14] M. Burgmair, M. Zimmer, I. Eisele, Humidity and temperature compensation in work function gas sensor FETs, Sens. Actuators B 93 (2003) 271–275.
[15] F. Pascal-Delannoy, B. Sorli, A. Boyer, Quartz Crystal Microbalance (QCM) used as humidity sensor, Sens. Actuators A 84 (2000) 285–291.
[16] B. Mumyakmaz, A. Özmen, M.A. Ebeoğlu, C. Taşaltın, İ. Gürol, A study on the development of a compensation method for humidity effect in QCM sensor responses, Sens. Actuators B 147 (2010) 277–282.
[17] C. Bernou, D. Rebiere, J. Pistre, Microwave sensors: a new sensing principle. Application to humidity detection, Sens. Actuators B 68 (2000) 88–93.
[18] C. Gomez-Yanez, C. Benitez, H. Balmori-Ramirez, Mechanical activation of the synthesis reaction of $BaTiO_3$ from a mixture of $BaCO_3$ and TiO_2 powders, Ceram. Int. 26 (2000) 271–277.
[19] P. Ferrer, J.E. Iglesias, A.P. Ayala, I. Guedes, A. Castro, Study of the Aurivillius phases $Bi_4Sr_{n-3}TinO_{3n+3}$ ($n = 4, 5$) synthesized by mechanochemical activation, Solid State Commun. 136 (2005) 621–626.
[20] J. Zhang, L. Gao, Synthesis of antimony-doped tin oxide (ATO) nanoparticles by the nitrate–citrate combustion method, Mater. Res. Bull. 39 (2004) 2249–2255.
[21] K. Tahmasebi, M.H. Paydar, The effect of starch addition on solution combustion synthesis of Al_2O_3–ZrO_2 nanocomposite powder using urea as fuel, Mater. Chem. Phys. 109 (2008) 156–163.
[22] A.B. Gaikwad, S.C. Navale, V. Samuel, A.V. Murugan, V. Ravi, A co-precipitation technique to prepare $BiNbO_4$, $MgTiO_3$ and $Mg_4Ta_2O_9$ powders, Mater. Res. Bull. 41 (2006) 347–353.
[23] X. Chu, H_2S-sensing characteristics of $Cd_2Sb_2O_7$ thick film sensor prepared by co-precipitation method, Mater. Sci. Eng. B 110 (2004) 103–106.
[24] A. Montenegro, M. Ponce, M.S. Castro, J.E. Rodríguez-Paez, SnO_2–Bi_2O_3 and SnO_2–Sb_2O_3 gas sensors obtained by soft chemical method, J. Eur. Ceram. Soc. 27 (2007) 4143–4146.
[25] T.R. Giraldi, M.T. Escote, A.P. Maciel, E. Longo, E.R. Leite, J.A. Varela, Transport and sensors properties of nanostructured antimony-doped tin oxide films, Thin Solid Films 515 (2006) 2678–2685.
[26] K.V. Gurav, V.J. Fulari, U.M. Patil, C.D. Lokhande, O.-S. Joo, Room temperature soft chemical route for nanofibrous wurtzite ZnO thin film synthesis, Appl. Surf. Sci. 256 (2010) 2680–2685.
[27] K.O. Rocha, S.M. Zanetti, Structural and properties of nanocrystalline WO_3/TiO_2-based humidity sensors elements prepared by high energy activation, Sens. Actuators B 157 (2011) 654–661.
[28] T.-S. Yang, C.-B. Shiu, M.-S. Wong, Structure and hydrophilicity of titanium oxide films prepared by electron beam evaporation, Surface Science 548 (1–3) (2004) 75–82.
[29] (a) H.C. Choi, Y.M. Jung, S.B. Kim, Size effects in the Raman spectra of TiO_2 nanoparticles, Vib. Spectrosc. 37 (2005) 33–38;
(b) W.F. Zhang, Y.L. He, M.S. Zhang, Z. Yin, Q. Chen, Raman scattering study on anatase TiO_2 nanocrystals, J. Phys. D: Appl. Phys. 33 (2000) 912–916.
[30] A. Gajović, M. Stubičar, M. Ivanda, K. Furić, Raman spectroscopy of ball-milled TiO_2, J. Mol. Struct. 563–564 (2001) 315–320.
[31] V.M. Longo, A.T. de Figueiredo, S. de Lázaro, M.F. Gurgel, M.G.S. Costa, C.O. Paiva-Santos, J.A. Varela, E. Longo, V.R. Mastelaro, F.S.D.E Vicente, A.C. Hernandes, R.W.A. Franco, Structural conditions that leads to photoluminescence emission in $SrTiO_3$: an experimental and theoretical approach, J. Appl. Phys. 104 (2008) 023515.
[32] J. Milanez, A.T. de Figueiredo, S. de Lazaro, V.M. Longo, R. Erlo, V.R. Mastelaro, R.W.A. Franco, E. Longo, J.A. Varela, The role of oxygen vacancy in the photoluminescence property at room temperature of the $CaTiO_3$, J. Appl. Phys. 106 (2009) 043526.
[33] B. Ravel, E.A. Stern, R.I. Vendrinskii, V. Kraizman, Local structure and the phase transitions of $BaTiO_3$, Ferroelectrics 206–207 (1998) 407–430.
[34] M. Kruk, M. Jaroniec, Gas adsorption characterization of ordered organic-inorganic nanocomposite materials, Chem. Mater. 13 (2001) 3169–3183.
[35] K.S.W. Sing, D.H. Everett, R.A.W. Haul, L. Moscou, R.A. Pierotti, J. Rouquérol, T. Siemieniewska, Reporting physisorption data for gas/solid systems with special reference to the determination of surface area and porosity, Pure Appl. Chem. 57 (1985) 603–619.
[36] N.V. Parizotto, K.O. Rocha, S. Damyanova, F.B. Passos, D. Zanchet, C.M.P. Marques, J.M.C. Bueno, Alumina-supported Ni catalysts modified with silver for the steam reforming of methane: effect of Ag on the control of coke formation, Appl. Catal. A: Gen. 330 (2007) 12–22.
[37] K. Nagaoka, K. Takanabe, Ken-ichi Aika, Influence of the reduction temperature on catalytic activity of Co/TiO_2 (anatase-type) for high pressure dry reforming of methane, Appl. Catal. A: Gen. 255 (2003) 13–21.
[38] P.R. Ettireddy, N. Ettireddy, S. Mamedov, P. Boolchand, P.G. Smirniotis, Surface characterization studies of TiO_2 supported manganese oxide catalysts for low temperature SCR of NO with NH_3, Appl. Catal. B: Environ. 76 (2007) 123–134.
[39] I.D. González, R.M. Navarro, W. Wen, N. Marinkovic, J.A. Rodriguéz, F. Rosa, J.L.G. Fierro, A comparative study of the water gas shift reaction over platinum catalysts supported on CeO_2, TiO_2 and Ce-modified TiO_2, Catal. Today 149 (2010) 372–379.
[40] N.V. Parizotto, D. Zanchet, K.O. Rocha, C.M.P. Marques, J.M.C. Bueno, The effects of Pt promotion on the oxi-reduction properties of alumina supported nickel catalysts for oxidative steam-reforming of methane: temperature-resolved XAFS analysis, Appl. Catal. A: Gen. 366 (2009) 122–129.
[41] A.P. Ferreira, D. Zanchet, J.C.S. Araújo, J.W.C. Liberatori, E.F. Souza-Aguiar, F.B. Noronha, J.M.C. Bueno, The effects of CeO_2 on the activity and stability of Pt supported catalysts for methane reforming, as addressed by in situ temperature resolved XAFS and TEM analysis, J. Catal. 263 (2009) 335–344.
[42] J.W.C. Liberatori, R.U. Ribeiro, D. Zanchet, F.B. Noronha, J.M.C. Bueno, Steam reforming of ethanol on supported nickel catalysts, Appl. Catal. A: Gen. 327 (2007) 197–204.
[43] S. Andonova, C.N. de Ávila, K. Arishtirova, J.M.C. Bueno, S. Damyanova, Structure and redox properties of Co promoted Ni/Al_2O_3 catalysts for oxidative steam reforming of ethanol, Appl. Catal. B: Environ. 105 (2011) 346–360.

Biographies

Sonia Maria Zanetti She received her PhD degree in Chemistry from UFSCar – São Carlos, Brazil, in 2001. She is researcher at IQ/UNESP – Araraquara – SP and consultant at SENCER LTDA. Her work has been mainly focused on ceramics applied as sensor.

Kleper de Oliveira Rocha He received his PhD degree in Chemical Engineering from UFSCar – São Carlos, Brazil, in 2009. He worked as researcher at SENCER LTDA and currently he is teacher at UNIPAM.

José Augusto J. Rodrigues PhD degree in Chemical Kinetics from the Université Pierre et Marie Curie – Paris V, France in 1996. Present work at INPE – National Institute for Space Research in partnership with PETROBRAS since 1980, developing materials and catalysts for satellite propulsion systems and combustion processes for CO_2 capture.

Elson Longo PhD degree in Chemistry from USP – São Carlos, Brazil. At present he is the coordinator of INTCM/LIEC (CNPq/FAPESP). His work is focused on materials chemistry.